

Award Number: W81XWH-15-1-0009

TITLE: Photovoltaic Retinal Prosthesis for Restoring Sight to Patients Blinded by Retinal Injury or Degeneration

PRINCIPAL INVESTIGATOR: Prof. Daniel V. Palanker

CONTRACTING ORGANIZATION: Stanford University  
Palo Alto, CA 94304

REPORT DATE: February 2016

TYPE OF REPORT: Annual

PREPARED FOR: U.S. Army Medical Research and Materiel Command  
Fort Detrick, Maryland 21702-5012

DISTRIBUTION STATEMENT: Approved for Public Release;  
Distribution Unlimited

The views, opinions and/or findings contained in this report are those of the author(s) and should not be construed as an official Department of the Army position, policy or decision unless so designated by other documentation.

REPORT DOCUMENTATION PAGE				Form Approved OMB No. 0704-0188	
Public reporting burden for this collection of information is estimated to average 1 hour per response, including the time for reviewing instructions, searching existing data sources, gathering and maintaining the data needed, and completing and reviewing this collection of information. Send comments regarding this burden estimate or any other aspect of this collection of information, including suggestions for reducing this burden to Department of Defense, Washington Headquarters Services, Directorate for Information Operations and Reports (0704-0188), 1215 Jefferson Davis Highway, Suite 1204, Arlington, VA 22202-4302. Respondents should be aware that notwithstanding any other provision of law, no person shall be subject to any penalty for failing to comply with a collection of information if it does not display a currently valid OMB control number. PLEASE DO NOT RETURN YOUR FORM TO THE ABOVE ADDRESS.					
1. REPORT DATE February 2016		2. REPORT TYPE Annual Report		3. DATES COVERED 1 Feb 2015 - 31 Jan 2016	
4. TITLE AND SUBTITLE  Photovoltaic Retinal Prosthesis for Restoring Sight to Patients Blinded by Retinal Injury or Degeneration				5a. CONTRACT NUMBER	
				5b. GRANT NUMBER W81XWH-15-1-0009	
				5c. PROGRAM ELEMENT NUMBER	
6. AUTHOR(S) Prof. Daniel Palanker  E-Mail: palanker@stanford.edu				5d. PROJECT NUMBER	
				5e. TASK NUMBER	
				5f. WORK UNIT NUMBER	
7. PERFORMING ORGANIZATION NAME(S) AND ADDRESS(ES)  Stanford University 452 Lomita Mall, Astrophysical Building, Stanford, CA 94305-4085				8. PERFORMING ORGANIZATION REPORT NUMBER	
9. SPONSORING / MONITORING AGENCY NAME(S) AND ADDRESS(ES)  U.S. Army Medical Research and Materiel Command Fort Detrick, Maryland 21702-5012				10. SPONSOR/MONITOR'S ACRONYM(S)	
				11. SPONSOR/MONITOR'S REPORT NUMBER(S)	
12. DISTRIBUTION / AVAILABILITY STATEMENT  Approved for Public Release; Distribution Unlimited					
13. SUPPLEMENTARY NOTES					
14. ABSTRACT Ocular trauma can result in traumatic retinopathy, which, like retinal degeneration, leads to blindness due to loss of photoreceptors. We are developing a photovoltaic subretinal prosthesis which directly converts light into pulsed electric current in each pixel, to stimulate the nearby neurons and thereby reintroduce visual information into retina. Images captured by the camera mounted on video goggles are projected onto retina by video goggles using pulsed near-infrared light. Modular design of these wireless arrays allows scalability to thousands of pixels, and combined with the ease of implantation, offers a promising approach to restoration of sight in patients blinded by retinal degenerative diseases. We propose to advance this remarkably successful technology towards clinical testing, including the following: addition of the biocompatible protective coating for long-term implantation in human patients, fabrication of the video goggles with a camera, image processing software and user interface for physicians and patients. If successful, photovoltaic retinal prosthesis with 70µm pixels is expected to provide visual acuity close to 20/200, and after the described preparations to the clinical use, will be commercialized in collaboration with an industrial partner.					
15. SUBJECT TERMS n/a					
16. SECURITY CLASSIFICATION OF:			17. LIMITATION OF ABSTRACT	18. NUMBER OF PAGES	19a. NAME OF RESPONSIBLE PERSON
a. REPORT	b. ABSTRACT	c. THIS PAGE			USAMRMC
Unclassified	Unclassified	Unclassified	Unclassified		19b. TELEPHONE NUMBER (include area code)

## Table of Contents

	<u>Page</u>
<b>1. Introduction.....</b>	<b>4</b>
<b>2. Keywords.....</b>	<b>4</b>
<b>3. Accomplishments.....</b>	<b>5</b>
<b>4. Impact.....</b>	<b>20</b>
<b>5. Changes/Problems.....</b>	<b>N/A</b>
<b>6. Products.....</b>	<b>N/A</b>
<b>7. Participants &amp; Other Collaborating Organizations.....</b>	<b>21</b>
<b>8. Special Reporting Requirements.....</b>	<b>N/A</b>
<b>9. Appendices.....</b>	<b>N/A</b>

## **Introduction**

Ocular trauma can result in traumatic retinopathy, which, like retinal degeneration, leads to blindness due to loss of photoreceptors. Sight can be restored to some extent by patterned electrical stimulation of the remaining inner retinal neurons. Photovoltaic subretinal prosthesis directly converts light into pulsed electric current in each pixel, stimulating the nearby neurons. Visual information is projected onto retina by video goggles using pulsed near-infrared (~900nm) light. Preparation of this technology for clinical trial requires optimization of the photovoltaic array, addition of the biocompatible protective coating for long-term implantation in human patients, fabrication of the video goggles with camera, and image processing software. In particular, we are working on (1) Development and testing of the SiC protective biocompatible coating for the implant. (2) Optimization of the pixel configuration to maximize its performance, such as light-to-current conversion efficiency, dynamic range, maximum repetition rate, and minimum cross-talk. (3) Development of the near-infrared pulsed video goggles. (4) Development of the image processing software and user interface.

### **Keywords**

Retinal prosthesis, photovoltaic, retinal degeneration, traumatic retinopathy, restoration of sight.

### **Major goals of the project**

#### **Major Task 1: Development and testing of the SiC protective biocompatible coating for the implant**

##### **Subtask 1**

- a) Coat the implant with amorphous SiC to prevent erosion.
- b) Test erosion of the coated and uncoated implants using accelerated aging at elevated temperature for 12 days, equivalent to 12 months at physiological conditions.
- c) Test erosion of the coated and uncoated implants in-vivo during 6-12 months.

##### **Subtask 2**

- a) Test biocompatibility of the SiC coating using subretinal implantation in the wild type (Long Evans) and RCS rats for 3-12 months. Retinal thickness and potential appearance of the subretinal gliosis or fibrosis will be monitored in-vivo using OCT. Health of the retinal vasculature and potential damage to RPE at the edges of the implant will be monitored using fluorescein angiography and autofluorescence.
- b) After enucleation, study retinal structure above the implant using confocal microscopy with immunohistochemical staining of the sample.
- c) In the case of poor biocompatibility we will add an additional layer of parylene on top of SiC, leaving only the electrodes exposed.

#### **Major Task 2: Optimization of the pixel configuration to maximize its performance, such as light-to-current conversion efficiency, dynamic range, maximum repetition rate, and minimum cross-talk.**

##### **Subtask 1**

- a) Using computational model of the equivalent optoelectronic circuit, optimize the number of diodes, sizes of the active and return electrodes and the exposed silicon area to maximize the output current, charge injection, and dynamic range of modulation.

- b) Using computational model of the equivalent optoelectronic circuit, optimize the value of the shunt resistor for sufficiently fast discharge between the pulses, while on the other hand, not draining too much current away from the tissue during the light pulse itself. The target frequency in this optimization corresponds to the perceptual flicker fusion observed in the range of 20-40 Hz.

#### Subtask 2

Using computational model of electric field in tissue, optimize connectivity of the return electrodes and the size of the metalized areas on the side and back walls of the implant to minimize the cross-talk of the neighboring pixels and to maximize the field penetration into the retina.

#### Subtask 3

- a) Manufacture optimized photovoltaic arrays
- b) Verify optoelectronic performance of the photovoltaic arrays experimentally in a saline solution.
- c) Verify optoelectronic performance of the photovoltaic arrays in-vivo by measuring electrical waveforms produced by the implant using corneal electrodes. The same animals with the subretinal implants will be used here, as the ones described in the Task 1/2/a

### **Major Task 3: Development of the NIR video goggles**

#### Subtask 1

- a) Develop video goggles with bright pulsed NIR (880-905nm) illumination.
- b) Ensure ocular safety in the event of a critical failure of the display.
- c) Assess the visual field, brightness and contrast of the projected images on the retina.

### **Major Task 4: Development of the image processing software and user interface**

#### Subtask 1

- a) Using information from our electrophysiological studies regarding spatial and temporal summation of the spot stimuli in a pattern, optimize the spatial and temporal sequence of the pixel activation to provide the highest dynamic range and contrast.
- b) Develop image processing to maximize the user's ability to accomplish daily tasks such as reading, face recognition, navigating an unfamiliar environment. Software should extract or enhance critical aspects of the image to be displayed in a crisper form to the user, such as text, simplified images of the objects matching the resolution limitations of the implant.

#### Subtask 2

- a) Develop the graphic user interface for the technician and for the patient. The GUI will allow adjustment of the image processing software, including the following parameters: (a) resolution, (b) dynamic range of brightness and the number of gray levels, (c) spatial filtering (edge enhancement, image sparsity, thresholding), (d) frame rate, sub-division of the frames, and pulse frequency.
- b) Evaluate a possibility of including the voice control and/or gesture recognition into the user interface.
- c) Test the image processing software and the user interfaces on healthy volunteers (3-4 members of the research team) using conventional video goggles with a similar visual field.

## **Accomplishments**

### **1. SiC Protective Coating for Photovoltaic Retinal Prostheses**

## Introduction

Photovoltaic retinal prosthesis for restoration of sight to patients blinded by degenerative retinal diseases [16-17] is exposed to body fluids. Without an optimized protective coating, the device remained functional in short-term (under 1 year) studies *in vitro* and *in vivo*, but with detectable degradation. For long-term use of this integrated circuit, a biocompatible encapsulation layer is necessary to provide stable protection against water and ion ingress.

Dielectric materials deposited by low-pressure chemical vapor deposition (LPCVD) at high temperatures (800-900°C) have exhibited good stability and barrier properties in long-term *in vivo* studies [19-21]. However, such temperatures are incompatible with encapsulation of ICs. Development of an encapsulation layer which can be deposited at temperatures below 400°C would be tremendously beneficial since it would allow its use for protection of ICs [22]. Low temperature (395°C) LPCVD silicon oxide (SiO<sub>2</sub>) implanted sub-retinally in rabbits was found to dissolve after 6–12 months [23]. Polymers, such as Parylene, are used in the medical industry for encapsulation of the neural implants [24-26]. Due to its low relative permittivity, high resistivity, biocompatibility and conformal deposition, Parylene is suitable as an electrical isolation material for implantable devices. Adhesion of Parylene to inorganic substrates can be improved by adhesion promoter and thermal treatment [27]. However, Parylene has relatively a high water vapor transmission rate (WVTR) compared to many dielectric materials [26,28], therefore Parylene by itself is not sufficient to protect implanted ICs. Atomic layer deposited (ALD) Al<sub>2</sub>O<sub>3</sub> is conformal and hermetic, yet found to dissolve in water [26,29]. An Al<sub>2</sub>O<sub>3</sub> and Parylene bilayer structure was proposed to improve its resistance to moisture and the encapsulation lifetime [26]. Diamond-like carbon (DLC) coatings [30] and ultra-nano-crystalline diamond (UNCD) coatings [31-33] have demonstrated biocompatibility, resistance to corrosion and wear, and are being used in medical implants, with some concerns regarding delamination in an aqueous environment caused by high residual stress, leakage current, pinholes near sharp corners, and a relatively high deposition temperature.

As an alternative, amorphous silicon carbide (SiC) deposited at a low temperature was proposed as a protective coating due to its availability in semiconductor processing, compatibility with IC technology, biocompatibility [34-36], contamination barrier properties [37-40] and low dissolution rate in saline, compared to other commonly used dielectric materials for IC passivation, such as silicon nitride (SiN<sub>x</sub>) and low-temperature SiO<sub>2</sub> [41-44].

In this study, we implanted retinal prosthetic devices for up to 1 year and characterized their degradation by optical and scanning electron microscopy (SEM) to assess the device failure mechanisms *in vivo*. We also measured the dissolution rates of SiC, SiN<sub>x</sub> and thermal SiO<sub>2</sub> in accelerated soaking tests to compare stability of those dielectric materials. We revealed and analyzed the defects in SiC films, and defined the optimal thickness of SiC layer for reliable protection of the chronic implants.

## Methods

### **Material deposition**

SiC was deposited by plasma-enhanced chemical vapor deposition (PECVD) at EIC Laboratories, Inc. (Norwood, MA). The precursors were SiH<sub>4</sub> and CH<sub>4</sub> (1:3 ratio of SiH<sub>4</sub>/CH<sub>4</sub>) in an Ar carrier gas. The deposition temperature was 325°C at a pressure of 800mTorr and an RF power frequency of 13.56MHz. The SiN<sub>x</sub> used in dissolution rate tests was deposited by PECVD at the Stanford Nanofabrication Facility (SNF) using Surface Technology Systems (STS) PECVD. The precursors were SiH<sub>4</sub> and NH<sub>3</sub> (40:33.5 ratio of SiH<sub>4</sub>/NH<sub>3</sub>) at a deposition temperature of

350°C and pressure of 650 mTorr. Dual frequency (13.56MHz and 187.5kHz) deposition was used. SiN<sub>x</sub> was deposited as the top surface coating of retinal prostheses by PECVD at SNF (Plasma-Therm Shuttlelock SLR-730-PECVD). This tool used a capacitive-coupled plasma with 13.56MHz RF power. Precursors were SiH<sub>4</sub> and NH<sub>3</sub> (5:3 ratio of SiH<sub>4</sub>/NH<sub>3</sub>), with He and N<sub>2</sub> carrier gases. The deposition temperature was 350°C at a pressure of 950mTorr. SiO<sub>2</sub> was grown by wet thermal oxidation in a resistance-heated oxidation furnace at 1000°C.

### Device fabrication

Three types of structures were used in this study. To minimize confusion, they are denoted as Type I, II and III, respectively.

Type I structures are retinal prosthetic implants fabricated at SNF using complementary metal-oxide-semiconductor (CMOS) and MEMS technologies. The fabrication process includes eight lithography steps on silicon-on-insulator (SOI) wafers with 30µm silicon device layers [45]. Each implant consists of an array of 142 hexagonal pixels, which are 70µm in width. An individual pixel contains 2 or 3 photodiodes connected in series between active and return electrodes. Photodiodes and pixels are isolated by 5µm-wide trenches filled with undoped polysilicon (Figure 1a). The implants are 1mm in diameter and 30µm thick. The main difference in the current devices from the previously described devices [45] is that the electrodes are connected to PN junctions with the opposite polarity – the active electrode connected to the p-type silicon region. This provides anodic-first pulses of current, optimal for sub-retinal stimulation [18,46]. Devices were fabricated on two wafers, both having 60nm of PECVD SiN<sub>x</sub> (Plasma-Therm) on top of 70-80nm of thermally grown SiO<sub>2</sub> (thermal oxide) on the surface. One wafer has an additional 240nm layer of SiC on the top surface.

The backside and sidewalls of all implants were covered with 480nm of thermally grown SiO<sub>2</sub>. Three Type I implants from each wafer were used in *in vivo* experiments. All of the 142 pixels of each implant were tested.

To facilitate defect analysis in SiC coatings, Type II structures were fabricated similarly to Type I devices but on bulk silicon

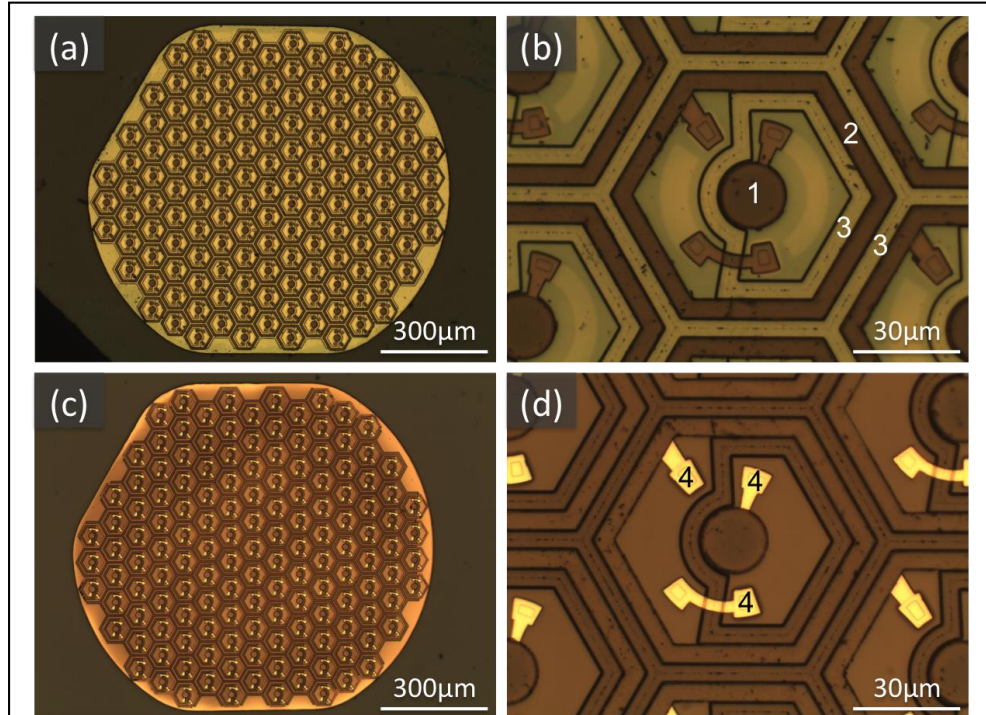


Figure 1: **Optical microscopy of retinal prostheses (Type I) without SiC coating.** (a) A 2-diode pixel device before implantation. (b) One pixel of the device in (a); 1 - active electrode, 2 - return electrode, 3 - trenches filled with polysilicon. (c, d) 4 months after sub-retinal implantation in a rat eye. The drastic color change and exposed metal wires (4, bright yellow) indicate the dissolution of SiN<sub>x</sub>.

wafers, making the total array thickness  $\sim 520\mu\text{m}$ . In addition to the  $240\text{nm}$  thick SiC films, some of Type II arrays had thicker SiC coating -  $560\text{nm}$ . These thick arrays were not used for *in vivo* experiments.

Type III structures are bulk silicon substrates ( $520\mu\text{m}$  thickness) with  $5\mu\text{m}$  wide and  $33\mu\text{m}$  deep trenches etched using the Bosch process (Surface Technology Systems STSetch2) at SNF. A thermal oxidation at  $1000^\circ\text{C}$  for 100 minutes followed the trench etching to conformally grow  $480\text{nm}$   $\text{SiO}_2$  on the samples. SiC films of  $560\text{nm}$  thickness were then deposited on the top surface of some samples, and  $180\text{nm}$ -thick SiC films were deposited on others. Type III structures were used for the defect analysis, but not for *in vivo* experiments.

### ***In vivo experiments***

Each of the six Type I retinal prostheses (three with SiC coating and three without) were implanted sub-retinally in a different rat (six rats in total). The implantation technique was similar to the one previously reported by our group [17,47] and performed in agreement with Stanford University institutional guidelines and the Statement for the Use of Animals in Ophthalmic and Vision Research. After a period of time (from 4 months to 1 year), implants were extracted from the tissue and cleaned in an enzyme solution (Tergazyme, 1%) for one day, and then further cleaned with deionized water and isopropyl alcohol (IPA). Explanted devices were examined with optical and scanning electron microscopy. Some devices were sputter coated with a thin layer of metal ( $\sim 10\text{nm}$ ) to improve the SEM imaging by reducing the charging effects. It was not always possible to compare the same device and the same pixel before and after the implantation due to randomness of the defect locations. However, each optical and SEM image is representative of the type of implant in terms of the device structure and changes after the implantation.

### ***Dissolution rate***

Dissolution rates of dielectric materials in saline were measured in accelerated soaking tests. SiC,  $\text{SiN}_x$ , and  $\text{SiO}_2$ -coated silicon substrates ( $520\mu\text{m}$  thickness) were sealed in glass vials filled with saline, and placed in an oven with the temperature maintained at  $87^\circ\text{C}$  for up to 112 days. Samples were periodically taken out of the chamber, rinsed with deionized water, dried and analyzed. The dissolution rate study at elevated temperature was performed in a low-phosphate saline (LPS), comprised of  $126\text{mM}$  NaCl,  $5\text{mM}$   $\text{Na}_2\text{HPO}_4$ , and  $1.4\text{mM}$   $\text{NaH}_2\text{PO}_4$ .

Five samples each of the SiC,  $\text{SiN}_x$  and  $\text{SiO}_2$  coatings were used in the accelerated aging tests. SiC and  $\text{SiN}_x$  were grown on double-side polished silicon substrates. Before the soaking test, the thickness of SiC and  $\text{SiN}_x$  films was directly measured by selectively etching away the dielectric materials in a small region and measuring the step using surface profilometry. SiC films were  $694\pm 10\text{nm}$  thick on each side, and  $\text{SiN}_x$  films were  $520\pm 5\text{nm}$  thick on each side.  $\text{SiO}_2$  were grown on single-side polished silicon substrates. Thickness of  $\text{SiO}_2$  films on silicon substrates was measured using spectral reflectometry (Nanometrics Nanospec 210XP), assuming the refractive index of  $\text{SiO}_2$  to be 1.45 in the visible range. The five  $\text{SiO}_2$  samples were found to be  $511\pm 3\text{nm}$  thick.

During the soaking tests of SiC and  $\text{SiN}_x$ , transmission-mode Fourier transform infrared spectroscopy (FTIR, Nicolet 6700) measurements were taken periodically on each sample to monitor changes of the films. The transmission FTIR spectra peaks were fitted, assuming Gaussian peak shapes, near the Si-C ( $\sim 758\text{cm}^{-1}$ ) or Si-N ( $\sim 820\text{cm}^{-1}$ ,  $930\text{cm}^{-1}$ ) stretch frequencies, and the areas under the peaks were integrated. Prior to the soaking tests, we calibrated the integrated areas of fitted Gaussian peaks measured by FTIR to the thickness measured by surface profilometry by linear regression on samples of 4 different thicknesses for both SiC and  $\text{SiN}_x$ . All subsequent FTIR peak areas were converted to film thickness using these fitted linear models. Assuming the



dissolution rates on both sides of the sample exposed to the same electrolyte are the same, the dissolution rate of a single exposed surface was calculated as half of the observed dissolution rate from two surfaces. For SiO<sub>2</sub> films, spectral reflectometry was performed periodically during the soaking test. The dissolution rate of each film was calculated by plotting the total film thickness versus soaking time.

### Defect analysis

Defect analysis was performed only on SiC films since all other coatings were gradually dissolving. To reveal the defects in the SiC films, Type II arrays were soaked in buffered oxide etch (BOE) 6:1 (volume ratio of 40% NH<sub>4</sub>F in water to 49% HF in water) for 10 minutes to etch SiN<sub>x</sub> and SiO<sub>2</sub> through any defects in the SiC films. After etching, the defects became visible under an optical microscope. Type III structures were analyzed similarly by etching materials underneath the SiC to reveal defects in the SiC films. Specifically, samples were soaked in BOE 6:1 for 7 minutes to etch SiO<sub>2</sub>. Some samples were further etched isotropically by xenon difluoride (XeF<sub>2</sub>) gas (Xactix e-1) to remove several microns of silicon. For cross-sectional SEM analysis of samples coated with 560nm SiC films, an additional SiO<sub>2</sub> etch in BOE 6:1 for 40 seconds was performed after cross sectioning the sample in order to recess the oxide and emphasize the SiC layer.

## Results

### Degradation of the implants in vivo

Implants without SiC coating degraded significantly during the 4-month sub-retinal implantation. SiN<sub>x</sub> layer was completely dissolved on all pixels and devices, which was evident from the color change of the devices after implantation (Figures 1c, d compared to 1 a, b). Platinum wires connecting the PN junctions to electrodes became exposed (Figure 1d). On one implant, polysilicon in the trench started to degrade, while on the other implant, this region did not show any visible changes.

All pixels without SiC coating implanted for 1 year showed visible degradation. However, the degradation was not uniform across a device, as shown in Figure 3a; some pixels exhibit more degradation than others. In some of the trenches, polysilicon was completely dissolved, leaving a thin SiO<sub>2</sub> membrane covering the trench top (Figure 2b, 1). As a result, the metal wires on top of these empty trenches were mechanically compromised (Figure 2b,

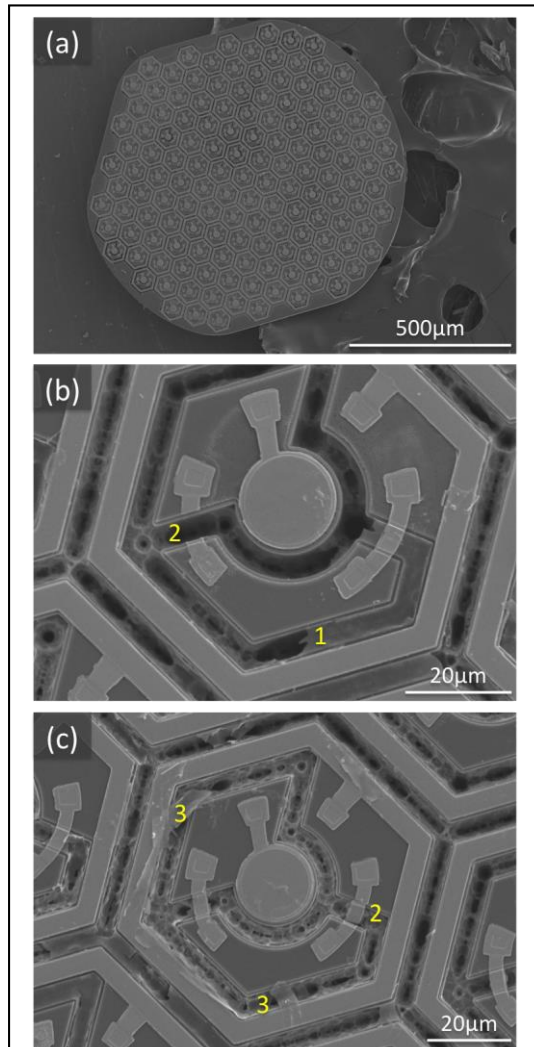


**Figure 2: Scanning electron microscopy of retinal prostheses (Type I) without SiC coating after 1-year implantation.** (a) All pixels in this device have visible degradation, albeit not uniform across the device. Both 3-diode pixels in (b) and (c) exhibit significant degradation. Polysilicon in some trenches is largely dissolved, leaving only a thin SiO<sub>2</sub> film covering the trench top (b1). Metal wires on top of the dissolved trenches could break (b2, c2). Some SiO<sub>2</sub> films that originally covered the trench top were displaced (c3).

2, and 2c, 2). Some thin SiO<sub>2</sub> films that originally covered the trench top were displaced after the polysilicon underneath was dissolved (Figure 2c, 2).

Despite the degradation, the implanted devices continued to function until they were explanted at least 7 months later [ref], indicating that the SiO<sub>2</sub> films with metal wires on top of the empty trenches were displaced only during explantation (Figure 2). Prolonged exposure of the implants *in vivo* will eventually lead to complete dissolution of the polysilicon in the trenches, which is likely to result in the loss of mechanical support, leading to device failure. During very long *in vivo* exposure, we speculate that the 70nm of SiO<sub>2</sub> will eventually dissolve as well [48]. Once the active area (single-crystal silicon) of the devices is exposed to physiological environment, the silicon is expected to dissolve rapidly [43], and the devices will eventually stop functioning.

To evaluate the protective properties of SiC, three devices with 240nm of SiC coating were implanted in three different rats for 4 months. One implant did not show any visible degradation under the optical microscope (Figure 3c, d). Two other implants had minor degradation at isolated defect points, visible as small patches of color change near the middle of the polysilicon-filled trenches (Figure 3e, f, arrows) compared to the image before implantation (Figure 3a, b). These defects were seen on 51 out of 142 pixels on one device, and 41 out of 142 on another. The patches of color changes indicate the presence of defects in the SiC films near the middle of the polysilicon-filled trenches, which allowed dissolution of the underlying SiN<sub>x</sub>.

**In summary,** unprotected retinal implants degrade during prolonged *in vivo* exposure, while SiC films provided effective protection of the implants.

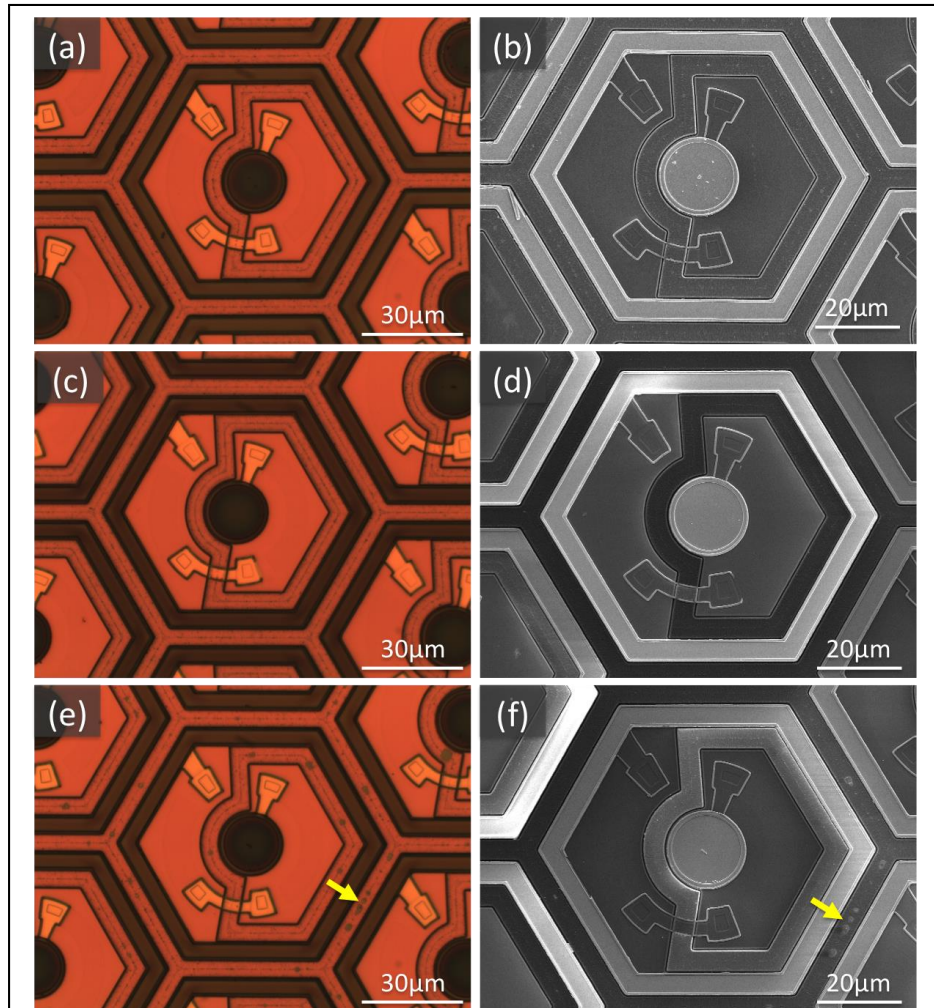


Figure 3: **Retinal prostheses (Type I) with 240nm SiC coating.** (a, b) A 2-diode pixel before implantation. (c-f) 4 months after sub-retinal implantation in a rat eye. (c, d) exhibits no signs of degradation, while (e, f) showed small patches of color change in the middle of the polysilicon-filled trench (arrows), indicating defects in the SiC film.

## 2. Modeling of Electric Field and Optimization of Return Electrodes in Neurostimulating Arrays

### Introduction

In neural circuits, information processing and transmission is associated with changes in the cellular transmembrane potential, which allows for recording and introducing information via electrode arrays. Therapeutic applications of electro-neural interfaces in the central and peripheral nervous system are rapidly expanding [1][2]. Cochlear implants [3] have seen the most remarkable success in sensory neuroprosthetics, while retinal implants [4][5] and various motor prostheses [6][7][8] are constantly improving.

Degenerative retinal diseases, such as retinitis pigmentosa and age related macular degeneration, cause blindness due to loss of photoreceptors [9][10], while the other two retinal neural layers remain fairly intact [11][12][13]. Retinal prostheses are designed to reintroduce visual information into the neural system by electrically stimulating the surviving neurons [14]. Two distinct approaches to retinal prostheses have been developed: (1) The subretinal approach targets the first layer of neurons after the photoreceptors (inner nuclear layer) composed primarily of bipolar and amacrine cells. (2) The epiretinal approach aims at stimulating the output cells of the retina (retinal ganglion cells, RGCs) whose axons form the optic nerve and relay visual signals to the brain. An epiretinal (Argus II, Second Sight Inc. [4][15]) and a subretinal (Alpha IMS, Retina Implant AG [16]) implants have been tested in clinical trials, and the Argus II is approved by FDA and CE for commercial use.

The subretinal and the epiretinal approach both rely on selectively stimulating the target neural layer. Direct stimulation of ganglion cells with epiretinal electrodes is designed to elicit an action potential in individual cells for each short ( $< 1$  ms) stimulus, and thereby could allow direct encoding of the ganglion cell output, completely bypassing the retinal neural network [17][18]. Individual ganglion cells can be targeted with the epiretinal electrodes by careful shaping of the electric field [19]. Subretinal stimulation utilizes longer pulses (1-10 ms) to activate graded-response cells in the inner nuclear layer, whose signals propagate via a network of synaptic connections to the ganglion cells, where they trigger bursts of action potentials. Unlike epiretinal stimulation, which directly encodes the strength of the RGC response by the number of delivered pulses or their frequency, strength of the graded response in the inner nuclear layer is encoded by stimulus amplitude or duration. The network-mediated stimulation preserves some features of natural vision, such as flicker fusion at high frequencies, adaptation to static images, and non-linear summation of subunits in the RGC receptive fields, which enables high spatial resolution [20].

To achieve spatial selectivity, both epiretinal and subretinal electrode arrays rely on precise shaping of the electric fields in tissue. The desired percepts are complex, and models of electric field need to account for the distributed effects of simultaneous activation of multiple electrodes in the array. Implants in clinical use today (Argus II and the Alpha IMS) use a common remote return electrode, and previous studies [21][22][23] indicate that cross-talk from neighboring pixels could strongly reduce the contrast of electrical pattern, and thereby limit the spatial resolution. Local spatiotemporal contrast of visual stimuli is a primary determinant of image perception [24][25], and decrease in the contrast transfer function from the camera to the stimulating electric field can negatively impact the prosthesis ability to convey meaningful visual information [26]. Poor confinement of electric field increases cross-talk between neighboring pixels, thereby lowering the contrast of the stimulation pattern. It is therefore crucial to quantify

the impact of various return electrode configurations on an implant's ability to deliver high contrast stimuli.

Contrast of electrical pattern can be quantified with respect to the potential or electric field (current density) in the medium. However, these quantities do not relate directly to neural stimulation efficiency in multi-layered tissue. Therefore, a model converting the generated electric field into retinal activity is necessary for analysis of the implant transfer function.

We demonstrate that modeling of electric field in electrolyte must take into account dynamics of the capacitive electrode-electrolyte interface, which rapidly transitions from an equipotential boundary condition at the beginning of a stimulation pulse to a uniform current density on electrodes in steady-state. When modeling a single stimulating electrode with a distant return, such change in boundary conditions has little effect. However, simultaneous activation of multiple electrodes in a dense array with local returns reveals the changes associated with this dynamic boundary condition. We verify the model by mapping the electric potential in electrolyte above the photovoltaic array with 70  $\mu\text{m}$  pixels.

We then quantify the differences in retinal response to electric fields generated by subretinal arrays with various return electrode configurations using a simple model of retinal response to network-mediated stimulation. Our results show that monopolar arrays with a common remote return have very poor field confinement. In an array with isolated local returns in each pixel, electric fields are over-confined, which prevents electric potential measurement on the corneal surface, thereby precluding post-implantation pixel diagnostics. An array with local returns in each pixel connected to one another provides a convenient compromise between these two extremes. Finally, we also demonstrate that dividing the input image into sparse sequentially-activated sub-frames [27] decreases the pixel cross-talk and increases the electric field contrast with little cost to stimulation selectivity.

## Methods

Methods are divided into two subsections: First, we define the procedures for modeling and measuring the electric field, including (1) HSPICE assessment of the dynamics of the boundary conditions, (2) COMSOL modeling of the spatial distribution of electric field in the medium, and (3) experimental field mapping. We then describe the method for converting the simulated electric field produced by subretinal array into retinal response.

### A. Modeling and Measuring Electric Field

#### *A1: Modeling in HSPICE*

High-density neurostimulating arrays include multiple active stimulating electrodes interleaved with a return electrode mesh [28], resulting in complex interactions between them. To assess the current redistribution dynamics between proximal and distal parts of the return electrode mesh, we model the system as a simplified equivalent circuit (Figure 1A) representing a single active disk electrode (1) surrounded by two concentric ring return electrodes (Figure 1B). The smaller adjacent ring (2) represents a local return immediately adjacent to the active electrode, while the larger and more distant ring (3) represents the rest of the return electrode mesh in the array. The electrodes coated with a sputtered iridium oxide (SIROF) are modeled as voltage-dependent capacitors, and interconnecting resistances ( $R_{xy}$ ) and resistances to infinity ( $R_x$ ) correspond to the electrolyte resistance [29]. A 5  $\mu\text{A}$  current source in the active branch provides 20 ms current pulses for this simulation.

Node *a* represents the active metal electrode potential. Potentials at nodes *b*, *c*, and *d* correspond to the medium just above the electrodes. Node *e* in this equivalent circuit represents a large Ag/AgCl reference electrode placed in electrolyte far from the electrode array. The potential



difference between nodes  $b$ ,  $c$ ,  $d$  and the reference node  $e$  represent the potential measured in the medium near each electrode surface (active, local return, and peripheral return, respectively), relative to the reference electrode.

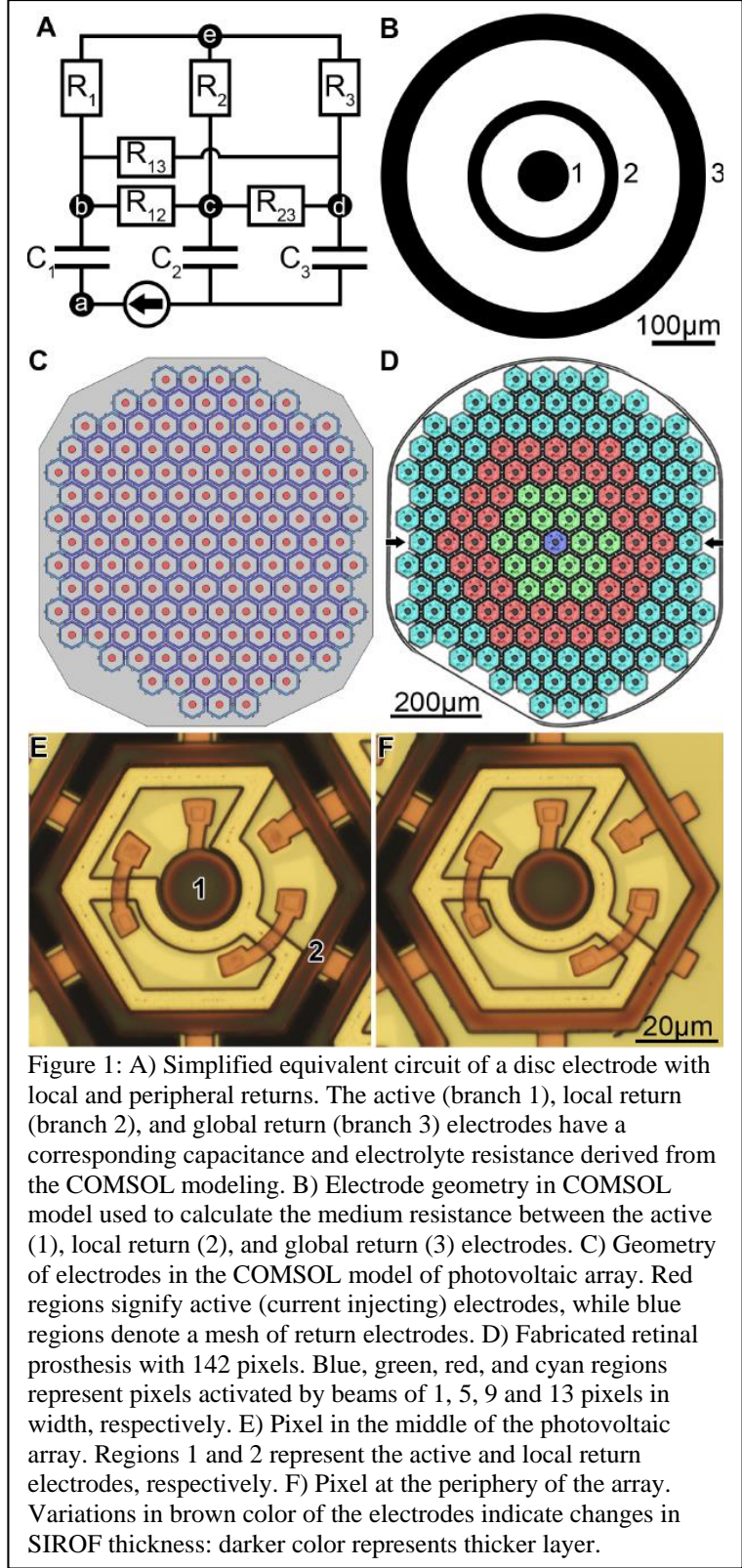
Interconnecting resistor values in the circuit were calculated using a finite element model solved in COMSOL Multiphysics 5.0, in which one electrode injects current  $I$ , while another electrode accepts the same current. The resistance between two electrodes is:

$$R_{xy} = \frac{V_x - V_y}{I}$$

Where  $V_x$  and  $V_y$  are potentials for the current injecting and returning electrodes of interest, respectively. We calculated the resistances between each electrode and the reference electrode at infinity, and then between each pair of electrodes: (1) the active (center) electrode and the local return; (2) the center electrode and the global return and (3) the local return and the global return. Resistive values from each electrode to infinity were calculated using the same model, but with the current  $I$  injected from an electrode and returning to a large equipotential boundary of the liquid domain at infinity. The resistance is then found by dividing the resulting potential at the electrode surface by the injected current.

#### A2: Electric Field in Electrolyte: Modeling in COMSOL

We assessed the electric field distribution in electrolyte in front of a photovoltaic array with various injected current patterns by solving a finite element model of the array in COMSOL Multiphysics 5.0, using the electrostatics module.



All COMSOL simulations were static, but the boundary conditions have been derived from the HSPICE simulation of the circuit dynamics.

We explored two boundary conditions for the stimulating and return electrodes: (1) When surface of each electrode was assumed equipotential, the COMSOL solver distributed the total injected current over each electrode such that the equipotential condition was met. (2) With the uniform current density boundary condition, the current density normal to the electrode surface was defined over each electrode by dividing the total injected current in each electrode over the corresponding electrode surface area. For both boundary conditions, we enforced charge balance by equating the total current at the return electrodes to the total current injected by the active electrodes. For all simulations, the zero reference voltage was set at the chamber sidewalls.

The modeled photovoltaic arrays are 1mm in diameter, 30  $\mu\text{m}$  thick, and are composed of 142 hexagonal pixels of 70  $\mu\text{m}$  in width [30][20][22][31] (Figure 1C). Each pixel has a central, 18  $\mu\text{m}$  diameter active disk electrode and 5  $\mu\text{m}$  wide hexagonal circumferential return electrode. Pixels are separated by 5  $\mu\text{m}$  wide gaps (Figure 1E). All electrode surfaces are coated with sputtered iridium oxide film (SIROF). The outer pixel ring (adjacent to the boundary of the array) has a thinner SIROF coating compared to the central pixels (notice the lighter color in Figure 1F), and therefore lower capacitance, compared to the rest of the array. Under the uniform current density boundary condition, the outer pixel ring accepts a lower current density compared to the rest of the returns, proportional to its capacitance per unit area (total charge balance over the array is still preserved), as explained in Section 3.2.

For comparison with experimental measurements, we computed electric fields in the electrolyte under four activation configurations (Figure 1D), corresponding to the light spot sizes on the photovoltaic array of 1, 5, 9 and 13 pixels in width.

#### *A3: Electric Potential Mapping in Electrolyte*

We validated our finite element model by measuring the potential generated in front of the photovoltaic array placed in a Petri dish filled with a 17.1mM NaCl solution (500 Ohm\*cm) and containing a large (1mm) Ag/AgCl reference electrode. A borosilicate micropipette (opening diameter 1  $\mu\text{m}$ ) containing the Ag/AgCl wire was positioned 20  $\mu\text{m}$  above the devices, and translated laterally and axially using a piezoelectric driver. Lateral translation of the pipette over the central row of the device (indicated by the arrows in Figure 1D) was performed with 2  $\mu\text{m}$  steps. Waveforms detected via the pipette electrode were recorded using a patch clamp amplifier (MultiClamp 700A, Axon Instruments). We averaged ten measurements at each position to improve the signal-to-noise ratio.

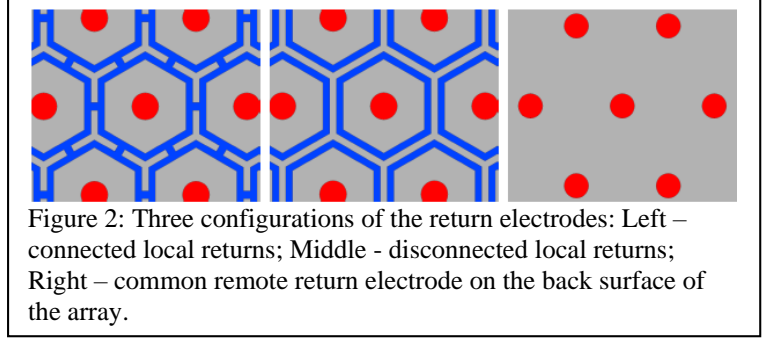
An 880nm laser (DILAS M1F4S22) illuminated the photodiodes with 5 ms pulses at 5 Hz repetition rate for all four spot sizes. The laser beam projected through an open iris via a 4x objective was sufficiently wide to illuminate the entire device, with a 10% intensity variation between the center and the periphery.

### **B. Modeling Retinal Stimulation**

#### *B1: Return Configurations*

We considered three different return electrode configurations in the array (Figure 2): connected local return mesh, isolated local returns, and monopolar array with a large common return at the back side of the implant. In the connected configuration, the 5  $\mu\text{m}$  wide hexagonal return electrodes surrounding each active electrode are electrically connected, creating a return electrode mesh that acts as a collective current sink. In the isolated configuration, individual pixel returns are not connected to their neighbors, and the current injected from the central active electrode is equal in value and opposite in sign to the current uniformly distributed over the

adjacent return electrode in each pixel. In the monopolar configuration, the return electrode covers the back side of the implant. Monopolar electrode arrays used in retinal prostheses usually have an even more distant return electrode (e.g. on a power supply of the implant), but for wireless photovoltaic pixels, the most practical place for a remote return electrode is on the back side of the device. For all configurations, we applied the uniform current density boundary condition on each electrode surface to represent device behavior in steady state.



### B2. Electric Field with Grid Patterns

Resolution and contrast sensitivity are often measured using grating patterns. We simulated the effect of grating patterns on the photovoltaic arrays by activating alternating pixel rows with various intensities:  $I_{max}$  (bright pixels) and  $I_{min}$  (dark pixels). In the common return configurations (connected and monopolar), the current flowing through the returns was equal to the total current injected through all active electrodes. Stimulating pattern contrast was defined by the Michelson contrast parameter

$$C = \frac{I_{max} - I_{min}}{I_{max} + I_{min}}$$

which varied between 0 and 1.

### B3: Modeling the Retinal Response

Activation thresholds for the RGCs and inner nuclear layer (INL) in terms of current density were taken from previously reported measurements of direct and network-mediated stimulation via large ( $> 500 \mu\text{m}$ ) electrodes [32]. Threshold was defined as the current density eliciting an action potential in retinal ganglion cells with a 50% probability at pulse duration exceeding cell chronaxy. With a 5 ms stimulus, the threshold was  $1\text{mA}/\text{cm}^2$  for direct RGC stimulation, and  $2\text{mA}/\text{cm}^2$  for the INL-mediated response. We assumed that only the vertical (z) component of the current density factors into the cell responsivity, and the middle row of the implant served as the region of analysis.

Strength of the network-mediated retinal response was expressed by the number of the elicited action potentials in RGCs, based on activation curve measured in rat retinas [28][20], which was scaled to match the threshold values with 50% response probability.

In degenerate rat retina (RCS), the INL extends between 5 and  $35 \mu\text{m}$  above the array, while the ganglion cell layer (GCL) extends between 80 and  $90 \mu\text{m}$  [33]. To asses retinal responses to electrical stimulation by each pixel, we multiplied the vertical current density at every point above the array by the corresponding INL responsivity value and integrated over the volume corresponding to the pixel size and thickness of the target cell layer (INL). For the network-mediated activation, the integration extended vertically from 5 to  $35 \mu\text{m}$ .

Direct stimulation of RGCs with epiretinal arrays and network-mediated stimulation with subretinal implants encode visual information differently: first by the number of pulses and their frequency, while the latter by the pulse amplitude and duration. Hence, selective activation of the INL or GCL is desirable for each strategy. For a subretinal implant, activation of the INL should avoid eliciting direct responses in RGCs. For each stimulation pattern, current density in the RGC layer should therefore remain below the direct stimulation threshold. Thus, for each device

configuration, the  $I_{\max}$  in the bright pixels was set to avoid direct stimulation of RGCs by ensuring the current density in the RGC layer stayed below  $1\text{mA}/\text{cm}^2$ .

The INL-mediated RGC activity in the bright and dark areas was calculated as the mean of the responses over bright and dark pixels along the middle row of the device, respectively:

$$N_{\text{bright}} = \frac{\sum_i^N N_{\text{bright}_i}}{N}$$

$$N_{\text{dark}} = \frac{\sum_j^K N_{\text{dark}_j}}{K}$$

where  $N$  and  $K$  represent the number of bright and dark pixels in the middle row ( $N=6$ ,  $K=5$ ), and  $N_{\text{bright}_i}$  and  $N_{\text{dark}_j}$  is the retinal responsivity for the  $i$ 'th and  $j$ 'th bright and dark pixel, respectively.

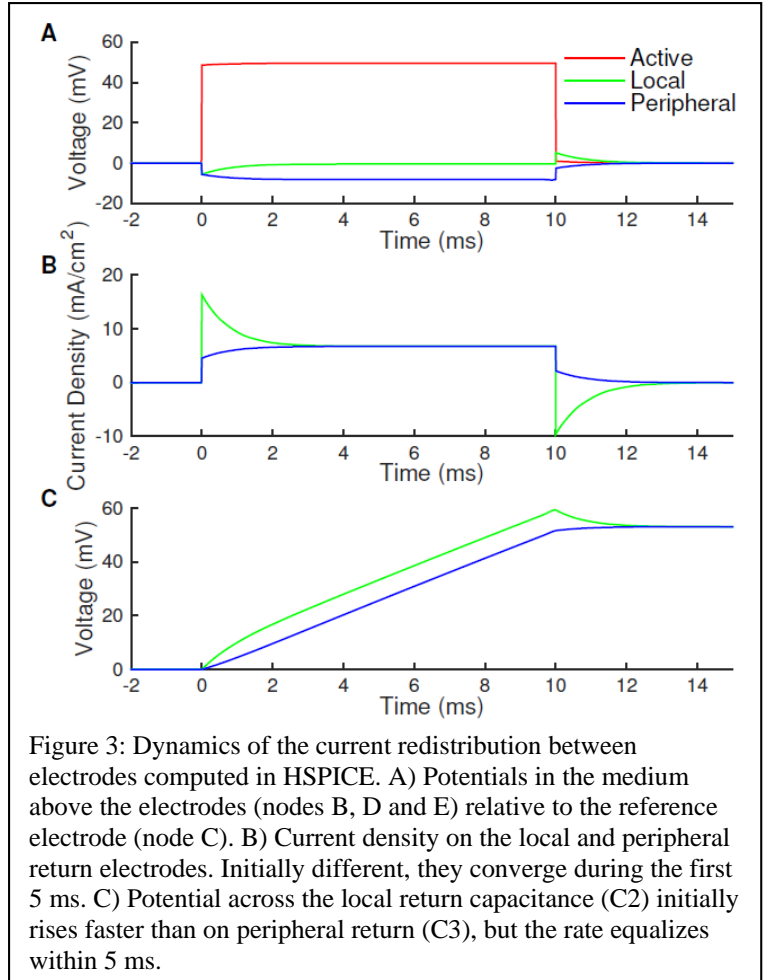
### III. RESULTS

#### A. Dynamics of current redistribution on an extended return electrode

Using the circuit shown in Figure 1A, we simulated the current redistribution dynamics during a stimulation pulse delivered into the medium via SIROF electrodes. With a central disk electrode of  $80\mu\text{m}$  in diameter, a local return electrode of  $200\mu\text{m}$  and  $240\mu\text{m}$  inner and outer diameters, and a peripheral return electrode of  $440\mu\text{m}$  and  $520\mu\text{m}$  inner and outer diameters, respectively, in a medium with  $0.2\text{S}/\text{m}$  conductivity ( $500\text{ Ohm}\cdot\text{cm}$  resistivity), the circuit parameters are:  $R_1 = 31.1\text{k}\Omega$ ,  $R_2 = 11.3\text{k}\Omega$ ,  $R_3 = 5.3\text{k}\Omega$ ,  $R_{12} = 30.7\text{k}\Omega$ ,  $R_{13} = 32.4\text{k}\Omega$ ,  $R_{23} = 10.4\text{k}\Omega$ ,  $C_1 \approx 50.3\text{nF}$ ,  $C_2 \approx 138\text{nF}$ ,  $C_3 \approx 736\text{nF}$ .

As shown in Figure 3A, the potentials above the local and peripheral return electrodes start deviating from the beginning of a pulse. Within about  $3\text{ms}$ , the potentials approach different steady state values of  $-0.5\text{mV}$  and  $-8.2\text{mV}$ .

As can be seen in Figure 3B, the local return initially accepts higher current density compared to the peripheral return. The smaller capacitance of the local return electrode is quickly charged, and therefore its potential rises faster than that of the larger peripheral return (Figure 3C). The potential rise rates and the corresponding current densities on return electrodes equalize within  $2\text{ms}$  (exponential time constant =  $0.8\text{ms}$ ), and remain constant for the rest of the pulse. If the electrode capacitance per unit area  $c$  is the same, the equal rates of the potential rise correspond to the same uniform current density  $j$  on each return electrode:





$$\frac{dV}{dt} = \frac{j}{c}.$$

However, if the capacitance per unit area of one return electrode is lower, the current density will be similarly reduced to provide the same rate of the potential rise. At the pulse end, electrodes are recharged following similar dynamics, but with an opposite polarity (Figure 3).

The current redistribution time course is set by the circuit time constant ( $t = RC$ ) with respect to the local electrode. For capacitance  $C = 51$  nF, and  $t = 0.8$  ms, the equivalent resistance seen by the local return electrode is 16 kW. Electrolytes with higher conductivities and electrodes with lower capacitance per unit area reach steady state faster. For example, electrodes with the same geometry as described above, but immersed in saline with higher conductivity ( $70 \Omega \cdot \text{cm}$  resistivity), reach steady state within 0.3 ms instead of 2 ms.

### B. Electric Field Produced by the Array

We measured electric potential in electrolyte  $20\mu\text{m}$  above the array having connected local returns after it reached the steady state. Potential measured across the central pixel row with four different activation spot diameters. To eliminate dependence on light intensity, the measured voltages for all spot sizes are normalized to the maximum voltage produced by the single pixel illumination. Increasing the activation spot size diameter from one to five pixels increases the maximum potential above the central pixel by a factor of 3. Further increase to a nine-pixel wide spot decreases the normalized potential in the center to 2.3, while illuminating the full array leads to a negative potential in the center.

Electric potential in the electrolyte calculated with a COMSOL model for two boundary conditions (equipotential and uniform current density) is shown in Figure 4 alongside the experimental measurements. The uniform current density model reproduces the initial increase and subsequent decrease of the potential in front of the device upon widening of the illumination spot. The model with equipotential electrodes, however, does not reproduce experimental results. In particular, the potential in front of the device does not increase enough with the partial illumination, and does not invert under the full-field illumination (Figure 4D).

The rise of potential with increasing beam size from one to five pixels results from two effects: (1) summation of the current from adjacent pixels, accounted for with both boundary conditions, and (2) an additional rise in the model with uniform current density due to the current spread over a wide return electrode mesh. Unlike very local return of current with equipotential electrodes, with uniform

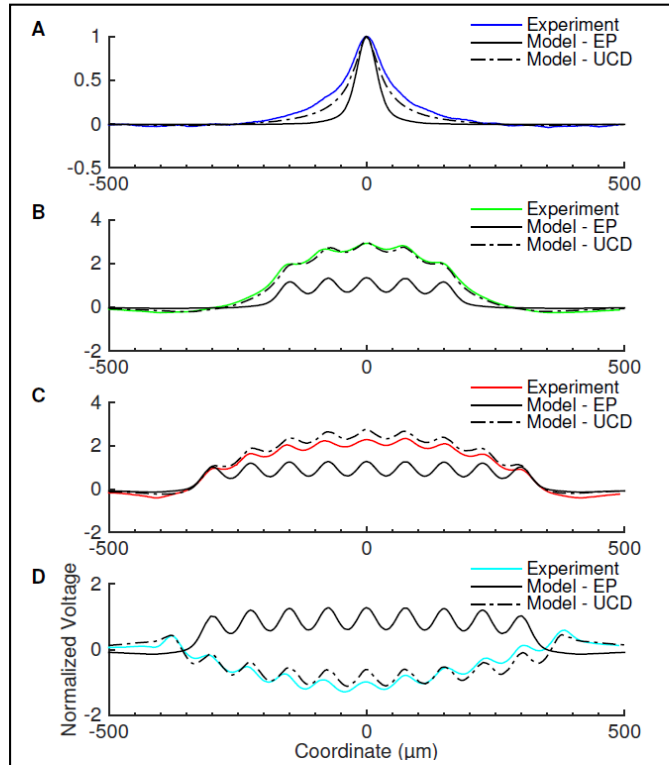


Figure 4: Comparison of the experimental results (color) with computational models utilizing an equipotential (EP, solid) and uniform current density (UCD, dash) boundary conditions for the beam sizes described in Figure 1D. Unlike with equipotential boundary conditions, modeling with the uniform current density matches all the features of the experimental data.

current density, the injected current spreads much further - over the entire device, resulting in an increase in of the potential above the active pixels.

When the number of active pixels increases further, the effect of the return electrode becomes more pronounced. Current density on the return electrode increases and its potential is drawn more and more negative. Illumination of the whole array (Figure 4D) produced negative potential in the center because the return electrode mesh around the peripheral pixels has a very low capacitance, which forces the current from these pixels towards the central portion of the return mesh. Devices with the same capacitance on all parts of the return electrode do not produce a negative potential in the center under full array illumination.

Current redistribution over the return electrode mesh depends on the extent of array utilization, i.e. on projected light pattern density and intensity. Therefore, the amplitude and contrast of the corresponding electrical pattern are affected by the projected image structure. We assess implications of these phenomena for retinal stimulation in the next section.

### C. Modeling Arrays with Various Return Configurations

Electric field distribution in front of the array is markedly different for bipolar and monopolar configurations (Figure 5). The absence of local returns in the monopolar array forces the injected current to flow to the back side, which results in a potential build-up in front of the device. Near each pixel (within the pixel radius), current spreads radially from the active electrode. Beyond the pixel radius, currents add-up and the whole array acts as one large electrode, with its electric field (current density) slowly decreasing with distance from the array (Figure 5C). Introducing local return electrodes eliminates this large potential build-up. The resulting current density and potential decrease much faster with distance from the array (Figure 5A,B).

In bipolar arrays with isolated returns, the injected current is drained back to the local return electrode in the same pixel, which confines the electric field much more than for the array with connected returns. In the latter case, current injected by a single active electrode can spread over the whole 1mm-wide return mesh. The wider current spread in this configuration results in a slower decrease of electric field with distance. A single activated pixel in the connected bipolar and monopolar arrays generates potentials 1mm away from the device that are two and three orders of magnitude greater than the potential generated by the isolated pixel, respectively. With electric field slowly decreasing with distance from the implant, it is possible to detect signals generated by single pixels on the cornea, which enables monitoring the pixels performance in the implanted arrays over time.

**Conclusions:** Extended electrodes transition from equipotential boundary conditions at the beginning of a pulse to uniform current density in steady state.

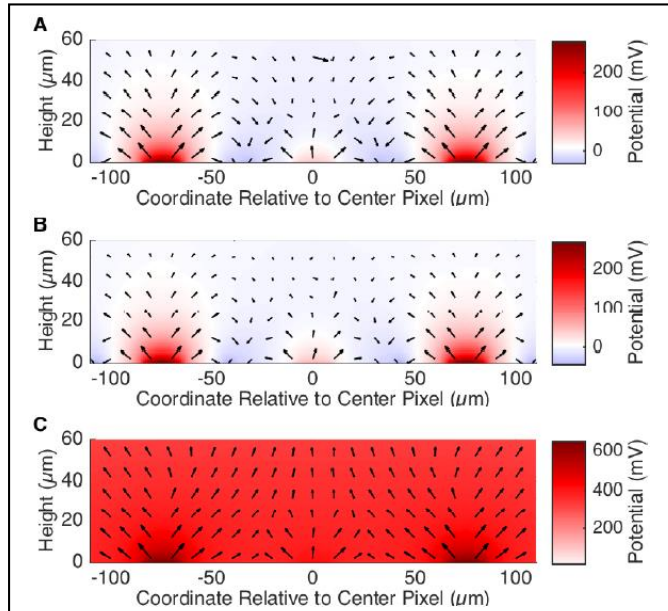


Figure 5: Potential (color map) and current (arrows) above the three peripheral pixels in the central row of the array. Due to reduced capacitance of the local return electrode at the edge of the array, peripheral pixels cannot locally return their injected current, and it flows towards the more central areas. This effect increases the negative potential of the returns in the center.

Electric fields generated by dense monopolar arrays with a remote return are poorly confined in axial direction, and therefore tend to indiscriminately activate all neural layers in the retina. A mesh of connected return electrodes surrounding each pixel confines the field and enables more targeted inner retinal stimulation, while avoiding direct activation of ganglion cells. An isolated local return electrode in each pixel provides the best field confinement, but it over-constrains the field to such an extent that it cannot be measured on the cornea, thereby preventing device diagnostics after implantation. Sequential activation of the stimulating electrodes may improve performance of the monopolar devices, and the extent of improvement depends on the number of simultaneously activated pixels.

## Dissemination of the Results

### Peer-reviewed publications

1. [Optimization of Return Electrodes in Neurostimulating Arrays](#). T. Flores, G. Goetz, X. Lei, and D. Palanker. *Journal of Neural Engineering* **13**: published online 21 April 2016.
2. [Implantation of Modular Photovoltaic Subretinal Prosthesis](#). D.Y. Lee, H. Lorach, P. Huie, D. Palanker. *Ophthalmic Surgery, Lasers and Imaging Retina*. **47**: 171-174 (2016).
3. [Retinal Safety of Near Infrared Radiation in Photovoltaic Restoration of Sight](#). H. Lorach, J. Wang, D.Y. Lee, R. Dalal, P. Huie, D. Palanker. *Biomedical Optics Express* **7**(1): 13-21 (2015).
4. [Interactions of Prosthetic and Natural Vision in Animals With Local Retinal Degeneration](#). H. Lorach; X. Lei; L. Galambos; T. Kamins; K. Mathieson; R. Dalal; P. Huie; J. Harris; D. Palanker. *Investigative Ophthalmology and Visual Science* **56**: 7444-7450 (2015).
5. [Contrast Sensitivity with a Subretinal Prosthesis and Implications for Efficient Delivery of Visual Information](#). G. Goetz, R. Smith, Xin Lei, L. Galambos, T. Kamins, K. Mathieson, A. Sher, and D. Palanker. *Investigative Ophthalmology and Visual Science* **56**: 7186–7194 (2015).
6. [Development of Animal Models of Local Retinal Degeneration](#). Henri Lorach, Jennifer Kung, Corinne Beier, Yossi Mandel, Roopa Dalal, Philip Huie, Jenny Wang, Seungjun Lee, Alexander Sher, Bryan William Jones, and Daniel Palanker. *Investigative Ophthalmology and Visual Science* **56**(8): 4644-4652 (2015).
7. [Photovoltaic Restoration of Sight with High Visual Acuity](#). H. Lorach, G. Goetz, R. Smith, X. Lei, Y. Mandel, T. Kamins, K. Mathieson, P. Huie, J. Harris, A. Sher, and D. Palanker. *Nature Medicine*, **21**:476–482 (2015).

### Conference presentations

1. Retinal safety of near infrared radiation in photovoltaic restoration of sight. Henri Lorach, Jenny Wang, Daeyoung Lee, Roopa Dalal, Philip Huie, Daniel Palanker; ARVO 2016
2. Implications of low prosthetic contrast sensitivity for delivery of visual information. Georges Goetz, Richard Smith, Xin Lei, Ludwig Galambos, Theodore Kamins, Keith Mathieson, Alexander Sher, Daniel Palanker; ARVO 2016
3. Robert and Gerry Ligon Lectureship at Vision Research Center, Kresge Eye Institute, Detroit. May 2016 “Photovoltaic Restoration of Sight in Rodents with Retinal Degeneration”

4. Annual Meeting of the Israeli Society for Vision and Eye Research. Ramat Gan, March 2016; "Photovoltaic restoration of sight in animals with retinal degeneration".
5. 20th Anniversary of the Institute of Photonics, University of Strathclyde, Glasgow, UK, November 2015. "OptoElectronic Restoration of Sight to the Blind".
6. Swedish Society for Bioengineering, Annual meeting, Uppsala, October 2015. "Optical and Electronic Approaches to Restoration of Sight".
7. 15th Euretina Congress, Nice, September 2015. "Prosthetic Restoration of Sight: Subretinal Approach".
8. Imaging and Applied Optics Congress of the Optical Society of America. Washington DC, June 2015. "Optical and Electronic Approaches to Restoration of Sight".
9. Massachusetts Eye and Ear Infirmary, Boston, MA, June 2015. "Non-Damaging Retinal Laser Therapy: mechanisms and applications"
10. Schepens Eye Research Institute, Harvard School of Medicine, Boston, June 2015. "Photovoltaic Restoration of Sight with High Visual Acuity".

**Impact:** Shear forces inflicted by explosion or head impact may result in traumatic retinopathy due to damage of the retinal pigmented epithelium and photoreceptors, leading to irreversible loss of sight. In these conditions the inner retinal neurons that process the visual signals and relay them to the brain are relatively well preserved. Patterned electrical stimulation of these neurons can elicit pattern perception, thereby restoring sight. Photovoltaic retinal prosthesis offers a very promising approach to restoration of sight due to its high resolution, wireless nature of the implants, small size, modularity and ease of implantation.

We continue advancing this technology according to the SOW, and transfer technology for commercialization and upcoming clinical trials by Pixium Vision. If successful, we expect the current implants to provide visual acuity on the level of 20/250. We are starting developing smaller pixels, which might enable visual acuity on the level of 20/120.

## Participants & other Collaborating Organizations

**Organization Name: Stanford University**

**Location of Organization: Hansen Experimental Physics Laboratory,  
452 Lomita Mall, Astrophysics Building,  
Room S05 & S04, Stanford, CA 94305-4085**

### 1. Prof. Daniel Palanker

Name:	Daniel Palanker
Project Role:	PI
Nearest person month worked:	1.8 CM
Contribution to Project:	Directs the project, evaluates the results, writes the reports and publications.

### 2. Mr. Philip Huie

Name:	Philip Huie
Project Role:	Research Associate
Nearest person month worked:	2.4 CM
Contribution to Project:	Helps with animal protocols, tissue processing and immunohistochemistry.

### 3. Mr. Ludwig Galambos

Name:	Ludwig Galambos
Project Role:	Research Associate/Engineer
Nearest person month worked:	4.2 CM
Contribution to Project:	Works on fabrication of the photovoltaic arrays

#### **4. Ms. Roopa Dalal**

Name:	Roopa Dalal
Project Role:	Research Associate (Histologist)
Nearest person month worked:	1.2 CM
Contribution to Project:	Works on tissue fixation, embedding, histological sectioning, staining and microphotography.

#### **5. Ms. Xin Lei**

Name:	Xin Lei
Project Role:	Graduate Student
Nearest person month worked:	3.0 CM
Contribution to Project:	Works on design and fabrication of the photovoltaic arrays.